CrossMark

ORIGINAL ARTICLE

Single pass fiber laser butt welding of explosively welded 2205/X65 bimetallic sheets and study on the properties of the welded joint

Ning-Nian Gou[1] · Jian-Xun Zhang[1] · Lin-Jie Zhang[1] · Zhen-Gang Li[1] · Zong-Yue Bi[2]

Abstract In this study, the explosively welded 2205 duplex stainless steel/X65 pipe steel bimetallic sheets were butt welded by a fiber laser in single pass. The microstructure, mechanical, and corrosion properties of the laser butt welded (LBW) joint were investigated. The results show that the upper fusion zone (FZ) is composed of the martensite and bainite phases, while the lower FZ is composed of austenite (A) and ferrite (F). Energy dispersive spectroscopy (EDS) test results indicate that only a small amount of Cr, Ni, and Mo migrated from the lower FZ to the upper FZ, whereas a small amount of Fe has been moved from the upper FZ to the lower FZ. During the tensile test process, The digital specklegram processing technology test results demonstrated that the fracturing of the specimens started at the lower FZ, and then the fracture grew towards the parent plates near the upper FZ. The face and root bend tests were carried out, and no separation, tearing, or fracture was observed around the joint. Accelerated corrosion test results show that the LBW joint has the superior corrosion resistance, but it has poor pitting corrosion resistance.

Keywords Bimetallic sheet · Single pass fiber laser butt welding · Microstructure · Mechanical property · Corrosion resistance

✉ Ning-Nian Gou
ningnian@stu.xjtu.edu.cn

✉ Jian-Xun Zhang
jxzhang@mail.xjtu.edu.cn

[1] State Key Laboratory of Mechanical Behavior for Materials, Xi'an Jiaotong University, Xi'an 710049, China

[2] Baoji Petroleum Steel Pipe Co., Ltd., Baoji, Shanxi 721008, China

1 Introduction

Bimetallic sheets can make full use of the two materials of their respective advantages to achieve the performance of which a single metal cannot provide. Generally, they are composed of a parent layer made of high-strength steel and a thin flyer layer of a corrosion-resistant alloy such as stainless steel [1] or titanium alloy as described by Chu et al. [2], which is put in close contact with the parent layer by some methods including casting [3], rolling [4], electromagnetic impact [5], and explosive welding. Explosive welding is one of the most widely used methods for producing bimetallic sheets. Raghukandan [6] produced a cu-low carbon steel plates by explosive welding and pointed out that the flyer thickness, the loading ratio, and the angle of inclination have significant contribution to the interfacial morphology of explosive clads, though the contribution of stand-off is not that severe. Gülenc [7] showed that aluminum could be well bonded to copper sheet by using explosive welding. Kahraman et al. [8] reported that the Ti6Al4V alloy plates and commercial copper plates can be bonded through explosive welding process and the strength of the interface was higher than that of the copper plate.

Bimetallic pipes can be fabricated from bimetallic sheets through multiple bending process (i.e., JCOE process) and longitudinal seam butting welding process. Such pipes find applications in petroleum engineering for long-distance transportation and refining of highly corrosive crude oil and natural gas. Usually, conventional pipeline steel, such as X65, is used as the parent layer, and stainless steel, such as duplex stainless steel 2205, is used as the material of the flyer plate layer in the bimetallic pipes. Using of the conventional pipeline steel as the parent layer offers high strength, high toughness, and low cost in the production of oil or gas transportation pipelines, while the stainless steel as the flyer layer offers excellent corrosion resistance, which can significantly increase the lifetime of the pipelines.

 Springer
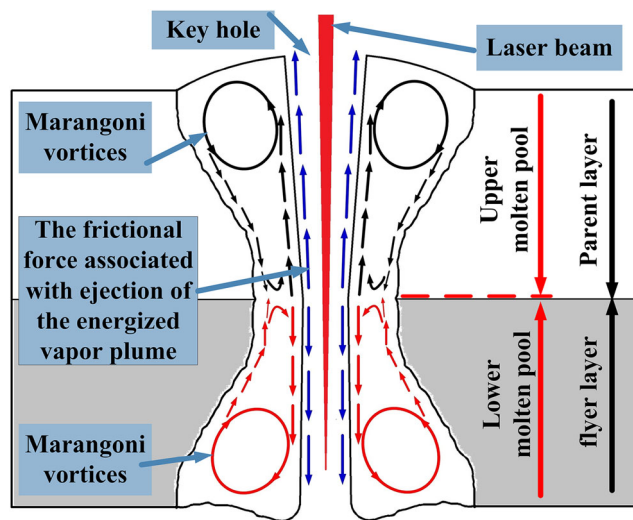
Fig. 1 Relationship between the flow behavior of the molten pool and the construction of bimetallic sheets

In this work, the 2205/X65 bimetallic sheet fabricated by the explosive welding technique was used to manufacture long oil and gas pipelines. This implied the sheet being subjected to multiple bending process (i.e., JCOE process) and longitudinal seam butt welding process in order to obtain a bimetallic pipe. Therefore, it is of great interest to jointing the bimetallic sheets. Torbatia et al. [9] welded the butting bimetal pipelines as pulse rapid arc gas metal arc welding (GMAW) was carried out from the outside of the pipe and autogenous gas tungsten arc welding (GTAW) was done from the inside. Chu et al. [2] jointed the explosive bonded CP-Ti/Q345 bimetallic sheets with multilayer (with different filler material) TIG welding method. Obviously, these traditional methods of bimetallic sheet butt welding have some imperfections which is inefficient and process complex. Compared with the previously used welding methods, the laser welding technique has higher welding speed, higher efficiency, and small welding deformation [10–12]. It is employed to produce joints of many materials, but it is hardly used for the bimetallic pipe production. Zhang et al. [13] indicated that the Marangoni convection played a critical role in determining the flow behavior of the molten pool during laser full-penetration welding. Zhang et al. [14] pointed out that the melt flow was also driven by the friction drag associated with the high-speed ejection of the energized vapor plume in full-penetration welding processes. Hence, the flow behavior of molten pool characterized as their relative independence of the upper and lower molten pool.

This independence is consistent with the independence of two materials for bimetallic sheets as shown in Fig. 1. In this study, based on the flow behavior of molten pool in full-penetration welding processes, the 2205/X65 bimetallic sheets were butt welded by a fiber laser with single pass. Furthermore, the microstructure and properties of the welded joint were studied through optical microscopy, scanning electron microscopy (SEM), energy dispersive spectroscopy (EDS), microhardness test, tensile test, bending test, and Tafel plot technique. The main goal of this study is to provide detailed information about properties of the LBW joints of bimetallic sheets, which can evaluate the performance of the joints, and the potential applications of single pass laser butt welding technology (without transition weld and higher welding speed) which can effectively simplify the welding procedure and raise welding efficiency for bimetallic sheets can be expanded.

2 Materials and methods

2.1 Materials and butt welding process

The material investigated is the explosively bonded 2205/X65 bimetallic sheets, with the flyer and the parent plates made of 2205 duplex stainless steel and X65 pipe steel, respectively. The thicknesses of the flyer and the parent plates were 2 and 16 mm, respectively. The chemical compositions of the flyer and the base plates are given in Table 1.

Laser butt welds were made on $100 \times 100 \times 4$ mm plates which were cut from the explosively bonded 2205/X65 bimetallic sheets. Figure 2 shows the process of the laser butt welding. A carbon dioxide laser operated in the continuous wave (cw) mode with a maximum output power of 4 kW was used. The optimal LBW parameters used for the welding were as follows: power, 4 kW; welding speed (v), 1.2 m/min; defocusing distance, 0.0 mm. Argon was used as a shielding gas flowing below and above the specimens with the rate of 20 L/min.

2.2 Metallographic studies

The butt welds' cross section was ground, burnished, and etched. The etchant comprised 100 mL alcohol, 100 mL HCl, and 5 g of CuCl2. A Nikon Eclipse MA200-type optical microscope was adopted for the microscopic studies.

Table 1 Chemical composition of X65 pipe steel and 2205 duplex stainless steel (wt%)

Materials	C	Si	Mn	P	S	Cr	Ni	Mo	N	Fe
2205	≤0.030	≤1.00	2.00	≤0.030	≤0.020	22.0–23.0	4.5–6.5	3.0–3.5	0.14–0.20	Balance
X65	0.046	0.24	1.6	0.099	0.017	0.0042	0.016	0.16	0.15	Balance
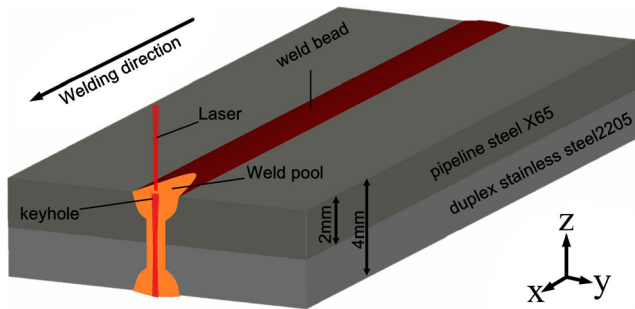
Fig. 2 Schematic sketch of 2205/X65 bimetallic sheet laser butt welding process

2.3 Mechanical tests

The microhardness test was executed employing a load of 300 gf and a remaining unchanged time of 10 s. A stratified tensile test and a full-thickness tensile test were carried out for the LBW joint and the bimetallic sheet that did not undergo laser butt welding. During the full-thickness tensile testing, the strain distribution in the welded joint was measured at a speed of 2 frames per second using a digital specklegram processing technology. The stratified specimens were collected using the method shown in Fig. 3, and the tensile specimens were then fabricated to the dimensions shown in Fig. 4. Both the face and the root bending tests for the full-thickness specimens were carried out under extreme conditions to reveal the weak points of the LBW joint. Finally, the joints in the bended specimens were examined.

2.4 Fracture observation

The fractures obtained from the full-thickness tensile tests were examined adopting a LS-JLLH-22 that scanned electron microscope. The LBW joint's fracture characteristics were analyzed by combining the metallographic examination consequences.

2.5 Corrosion test

Both the flyer layer (2205) of the bimetallic sheets and the lower surface of the LBW joint were subjected to an accelerated corrosion test based on Tafel plot technique. In this context,
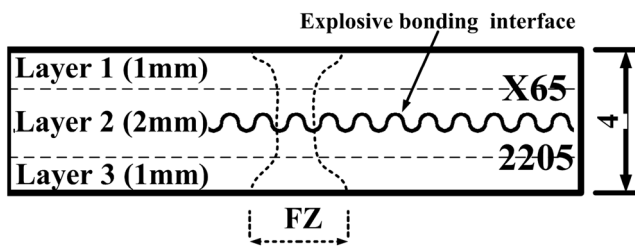
Fig. 3 Stratified scheme for stratified tensile test for bimetallic sheet and LBW joints (units: mm)
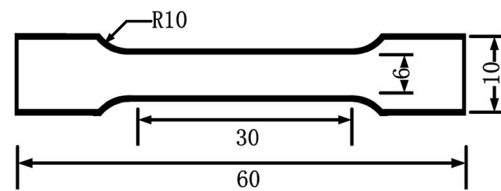

Fig. 4 Dimensions of the tensile and the stratified tensile specimen (units: mm)

the samples were first cut in 4×4 mm squares, polished, and mounted with an epoxy resin on an electrode holder. The test was conducted in a 0.35 wt% NaCl solution under open circuit condition for 60 min until E-corr becomes constant. Then, a potential was applied through the specimen for another 30 min in order to measure the relation between the potential and the current, from which the corrosion rate was deduced.

3 Results and discussion

3.1 Optical microstructure

Figure 5 shows cross-sectional macrographs of the LBW joint, produced using the above-mentioned parameters. These welding parameters resulted in a fusion zone (FZ) featuring a deep penetration and the typical "X" shape which is a characteristic of the LBW fusion zone. It is notable that the FZ is symmetrical about the laser beam's axis and the weld profile was obtained where the FZ interface is a smooth curve with no inflections. This symmetry implies steady convective heat transfer and steady fluid flow. The heat-affected zone (HAZ) and the base metal (BM—bimetallic sheet in this paper) was approximately identified in terms of the microstructural difference from Fig. 5. It can be seen that the overall widths of the HAZ is around 0.5–1 mm on the X65 side and 0.1–0.3 mm on the
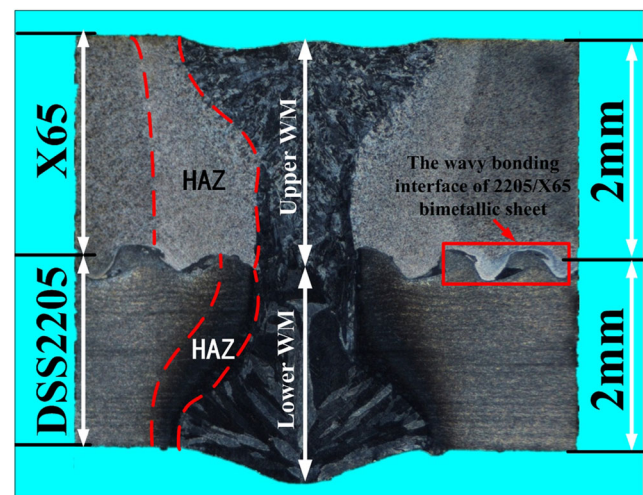
Fig. 5 Cross-sectional view showing different welding regions of the welded joint

Fig. 6 Optical microscopy images of the cross section of the welded joint: *(a)* cross-sectional view of the welded joint, *(b)* high-resolution image (HRI) of position b in *(a)*, *(c)* HRI of position c in *(a)*, *(b1)* fusion zone in *(b)*, *(b2)* coarse-grained region in *(b)*, *(b3)* fine-grained region in *(b)*, *(b4)* base metal in *(b)*, *(c1)* fusion zone in *(c)*, *(c2)* heat-affected zone in *(c)*, *(c3)* base metal, *(d)* position d in *(a)*, *(d1)* position d1 in *(d)*, *(d2)* position d2 in *(d)*
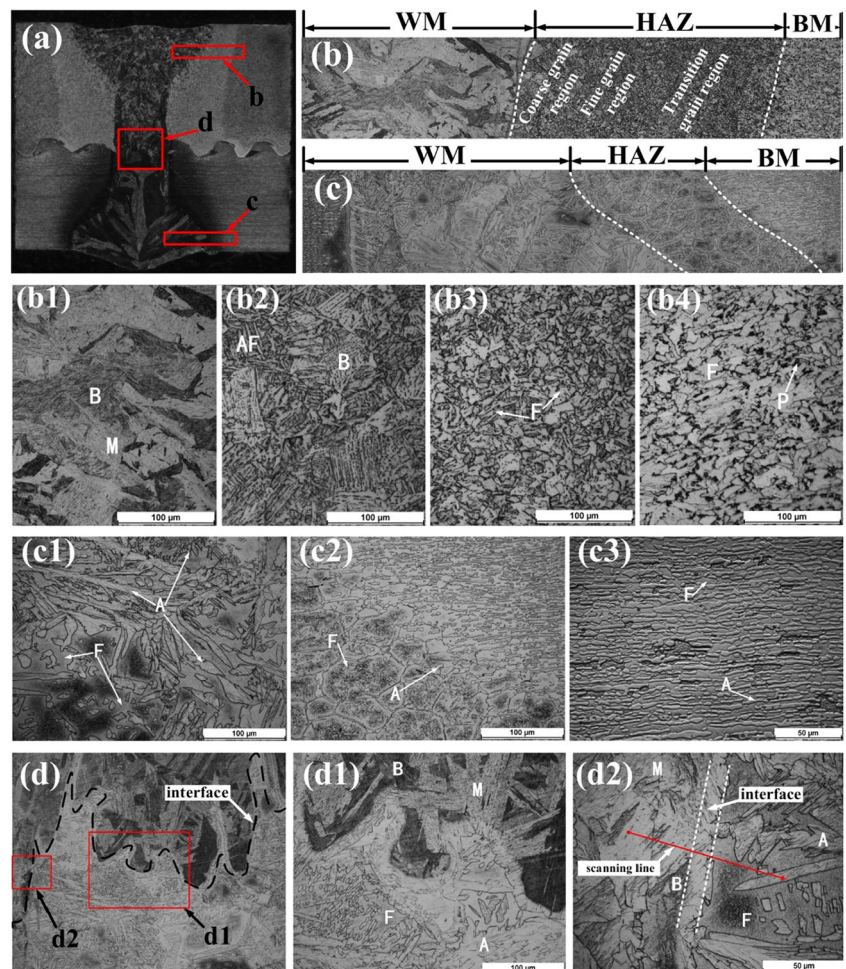

2205 side, respectively, which is due to different thermal conductivity of X65 and 2205. Figure 5 also shows that the macroscopic morphology of the crystal is different for the upper FZ and for the lower FZ, and the two kinds of crystal structure form staggered hybrid in the middle of FZ that is different from the bonding interface of 2205/X65 bimetallic sheet, having a wavy morphology as indicated by the red rectangles in Fig. 5.

Figure 6 shows the metallographic structures of the welded joint's cross section at three typical regions, which are marked by the rectangles b, c, d in Fig. 6a. Figure 6b illustrates that the variety of microstructures in region b includes HAZ, BM, and FZ at the joint's upper part. Higher resolution images that are revealed in Fig. 6b2, b1, b4, and b3 correspond to CGHAZ, FZ, and BM phases and FGHAZ in this region. Figure 6c shows that the variety of microstructures in region c is composed of HAZ, BM, and FZ at the joint's lower part. Higher resolution images in Fig. 6c2, c3, and c1 correspond to HAZ, BM, and FZ in this region. Figure 6d shows the microstructures of the region d, as indicated by the rectangle d in Fig. 6a

Figure 6b1 shows that martensite appears in the upper FZ (X65 side) due to high cooling rate, resulting in the higher average hardness (as shown in Fig. 7) with respect to BM

(X65) and HAZ (X65). Figure 6b1 shows that the microstructure consists of polygonal ferrite (PF) and quasi-polygonal (QF) ferrite. The PF grains have equiaxed, smooth, and
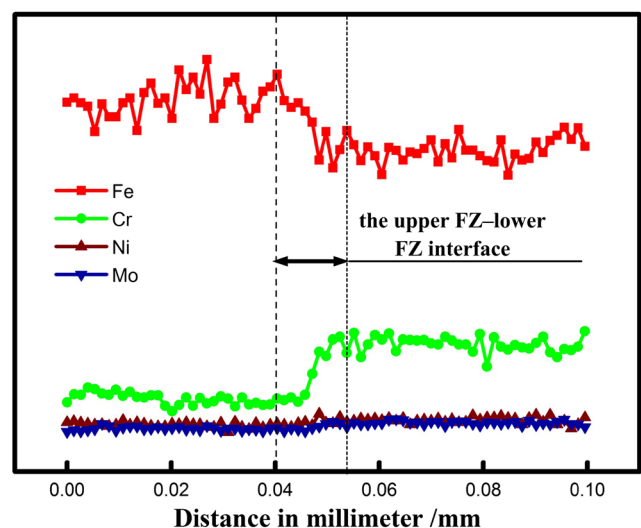
Fig. 7 EDS line scan showing variation of alloying elements across the upper FZ-lower FZ interface

Fig. 8 EDS analysis results of local FZ: *(a)* results for rectangle 1 in *(e)*, *(b)* results for rectangle 2 in *(e)*, *(c)* results for rectangle 3 in *(e)*, *(d)* results for rectangle 4 in *(e)*, *(e)* target areas of EDS analysis
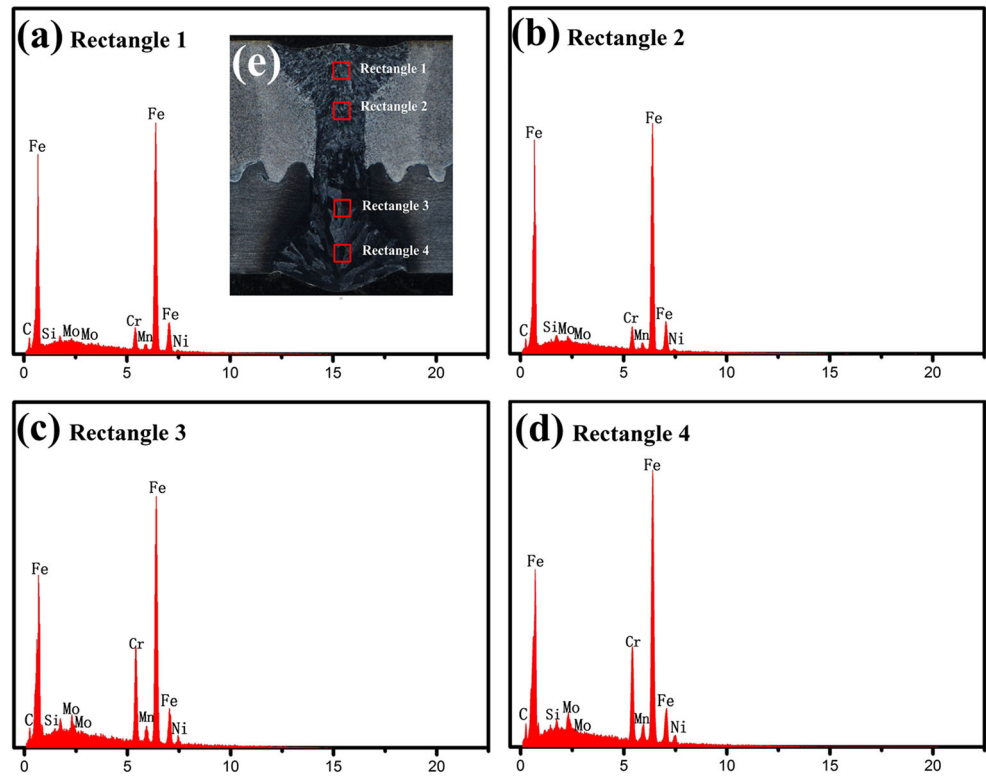
continuous boundaries, and the QF grains have irregular and jagged boundaries, containing subboundaries. Figure 6b1 and b2 illustrate both the coarse-grained (CG) and fine-grained (FG) HAZ microstructure. These zones consist of bainite, polygonal, and acicular ferrite. Figure 6b4 shows that the BM (X65 side) has a fine-grained microstructure consisting of bainite and acicular ferrite, as reported by Srinivasan et al. [15].

Figure 6c shows the microstructure of the lower part of the joint. The noticeable feature of the microstructure in the lower FZ (2205 side) is the highly directional nature around the axis of the laser beam as shown in Fig. 6a. This is due to solidification of the FZ at a high cooling rate. Fig. 6c1 shows that the lower FZ's (2205 side) microstructure consists of networks of austenite (A) at ferrite grain boundaries and intragranular austenite (A) precipitates that was embedded in the continuous ferrite (F). The high cooling rate associated with the laser welding process resulted in the formation of excessive amount of ferrite in the lower FZ (F/A ratio = 65/35). This unbalanced F/A ratio was partly attributed to high cooling rate of laser

welding process and the reduction of the nitrogen content in the lower FZ, as referred by Young et al. [16].

It can be seen that the lower HAZ (2205 side) is just about 0.2-mm wide (Fig. 6c2). In this zone austenite is present as grain boundary allotriomorphs along the ferrite grain boundaries, where intragranular austenite precipitates. This implies that the HAZ peak temperature is sufficiently high to promote austenite's partial transformation to ferrite during welding. In this way, the original ferrite/austenite balance becomes highly disturbed. A high content of dark intragranular etching agent is also apparent in both lower FZ (2205 side) and lower HAZ (2205 side) microstructures. It is believed that these precipitates result from formation of chromium rich intermetallic when

Table 2 Normalized chemical composition (wt%)

Rectangle	Fe	Cr	Ni	Mo
1	85.93	4.28	1.35	0.59
2	89.98	4.73	1.45	0.52
3	71.07	15.36	3.96	2.35
4	71.69	14.75	3.72	2.22
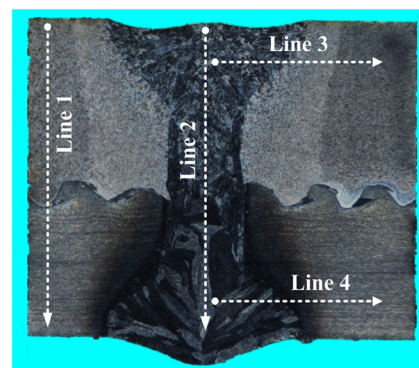
Fig. 9 The test position of the Vickers hardness test line on the cross section
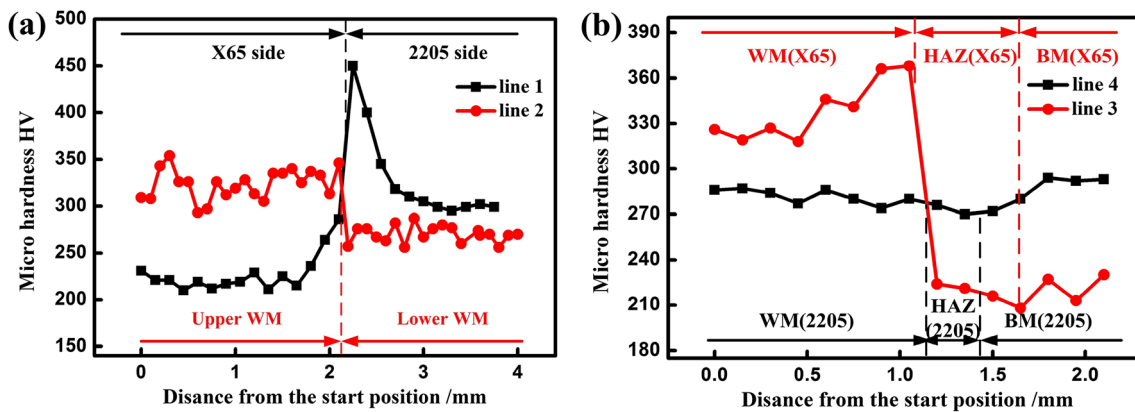
Fig. 10 **a**, **b** Results of the microhardness profile on the cross section

cooling below the ferrite melting temperature as described by Yang et al. [17]. Mourad et al. [18] described that these precipitates form a brittle and hard phase, which can decrease the toughness, corrosion resistance, and ductility of the 2205 welded joints.

Figure 6d reveals that there is a clear interface between the lower FZ and the upper FZ in the middle of FZ. On a high-resolution image shown in Fig. 6d1 (position d1 in Fig. 6d), it can be seen that the interface is a region of about 18-µm wide. This region's presence is attributable to the differences in the crystal structure between X65 and 2205, which are similar to the report of Sadeghian et al. [19], and, furthermore, according to Srinivasan et al. [20] and Liu et al. [21], it can be due to the transition in primary solidification behavior that is caused by the compositional gradient between the two materials. EDS line scan was performed at the interface, and the scan line's position is shown in Fig. 6d2 (position d2 in Fig. 6d). The result of the line scanning is shown in Fig. 7, where the concentration gradient of alloying elements across this interface is visible. The content of Cr, Mo, and Ni is increasing and the content of Fe decreases gradually across the upper FZ-lower FZ interface. The constituent gradient of Cr is steeper than that of Mo and Ni.

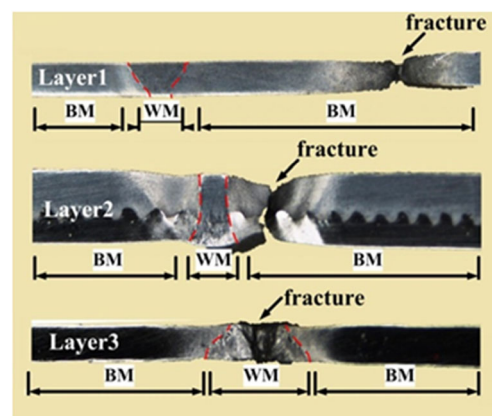**3.2 Distribution of alloy elements across the welded joint**

Figure 8 shows the EDS analysis results of four regions (as indicated by the rectangles 1, 2, 3, and 4 in Fig. 8e) on the cross section of the LBW joint. As shown in Fig. 8e (inset in Fig. 8a), regions 1 and 2 are located on the upper FZ while regions 3 and 4 are located on the lower FZ. Table 2 shows the detailed test results for the alloy element composition of the four regions. It shows that region 1 is composed of 0.59 wt.% Mo, 1.45 wt.% Ni, and 4.73 wt.% Cr, sharing similar element composition with region 2, while region 3 is composed of 2.22 wt.% Mo, 3.72 wt.% Ni, and 15.75 wt.% Cr, sharing similar element composition with regions 4. Comparing Tables 1 and 2 also illustrated the elemental migration across the LBW joint. It was observed that only a small amount Cr,

Ni, and Mo has been migrated from lower FZ to upper FZ whereas a small amount Fe has been moved from upper FZ to lower FZ. Such diffusion of a small amount of elementals can be attributed to the Marangoni vortices caused by the surface tension forces near the upper and the lower surfaces of the laser molten pool as demonstrated by Bachmann et al. [22].

3.3 Mechanical properties

3.3.1 Microhardness

Figure 9 shows the test position of the Vickers hardness test on the cross section of the LBW joint. The results in Fig. 10a show a remarkable difference in the microhardness between BM (test line 1) and WM (test line 2). In Fig. 10a, test line 1 demonstrates that the microhardness generally decreases as the distance from the explosive welding interface increases, which are similar to the report of Findik [23]. It is generally accepted that this effect can be attributed to the high plastic deformation in the explosive welding zone as compared to the area further away. The maximum Vickers hardness of X65 near the interface was approximately 300 HV, which was approximately 33 % higher than the 225 HV hardness of X65 far

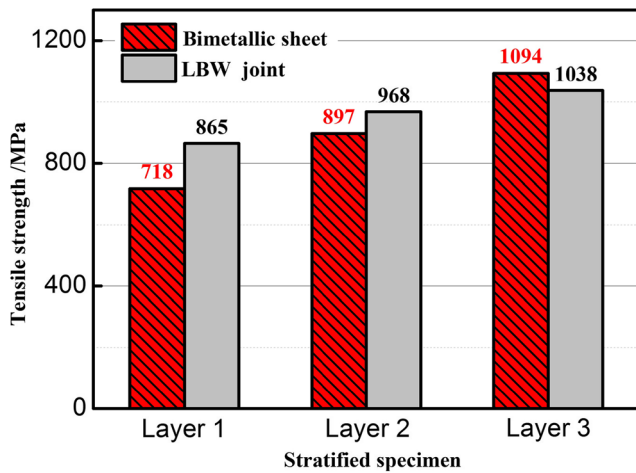**Fig. 11** Stratified tensile test specimen after stratified tensile test

Fig. 12 Stratified tensile test results for bimetallic sheet and LBW joint

the 2205 side is about 300 HV. HAZ and FZ revealed little lower hardness values, 280 HV for FZ and 280–270 HV for HAZ. The hardness profiles generally reveal that there is no significant difference between hardness of BM and that of FZ or HAZ (i.e., 300–325 HV), the variation's inspite in ferrite/ austenite ratio.

3.3.2 Tensile test

Figure 11 shows the corresponding LBW samples (after tensile test) for stratified tensile test. Figure 12 summarizes the pattern of variation in the tensile strength of the LBW joints and of the bimetallic sheet. Figure 12 shows that after LBW the tensile strength of layer 1 (i.e., X65) increased from about 718 to 865 MPa, and the failure occurred far away from FZ (see Fig. 11). The tensile strength of layer 2 was approximately 968 MPa, and the failure occurred away from the FZ (see Fig. 11). The tensile strength of the layer 3 (i.e., 2205) decreased from 1094 to 1038 MPa, and the failure occurred on the FZ (see Fig. 11).

Figure 13a shows the stress-strain curves of tensile test for the full-thickness LBW joint, and the corresponding strain distributions in the LBW joints during the tensile monotonic loading are shown in Fig. 13b. Figure 14a shows the stress-strain curves of tensile test for the bimetallic sheet, and the corresponding strain distributions in the bimetallic sheet during the tensile monotonic loading are shown in Fig. 14b. From Figs. 13b and 14b, it can be seen that the plastic strain evolution of the specimens can be divided into two stages: inhomogeneous deformation and homogenous deformation. When the tensile time is below point A, the strain distribution in the specimens is homogenous, which suggests a homogenous deformation stage. The specimens' strain heterogeneousness rises, which indicates an inhomogeneous deformation stage, as the tensile time rises. For the bimetallic sheet, as revealed in Fig. 14b, as the tensile time rises, the specimen undergoes an extremely localized deformation, which results in cracking and, finally, to fracturing. A fracture of the tensile test

away from the interfacial region. The maximum Vickers hardness of 2205 near the interface was approximately 450 HV, which was approximately 50 % higher than the hardness of 2205 of 300 HV far away from the explosive welding interface region. In Fig. 10a, test line 2 shows the microhardness distribution in the FZ of the LBW joint. Here, the microhardness of the upper FZ changed slightly, and the average hardness was approximately 334 HV, which is approximately 43 % higher than the hardness of BM (X65 side) of 230 HV. This is attributed to the formation of a large number of martensite laths under the high cooling rate of the LBW. As for the lower WM, the microhardness changed slightly too, and the average hardness was approximately 270 HV, which is slightly lower than the hardness of BM (2205 side) of 290 HV.

In Fig. 10b, test line 3 and test line 4 show the microhardness distribution from FZ to BM on the X65 side and the 2205 side of the LBW joint, respectively. Test line 3 shows that the FZ on the X65 side displays the highest hardness owing to martensite's formation. The hardness values decrease rapidly in HAZ. The average hardness of BM on the X65 side is approximate 210 HV, while the average hardness in the FZ is 344 HV. Test line 4 shows the microhardness of the BM on
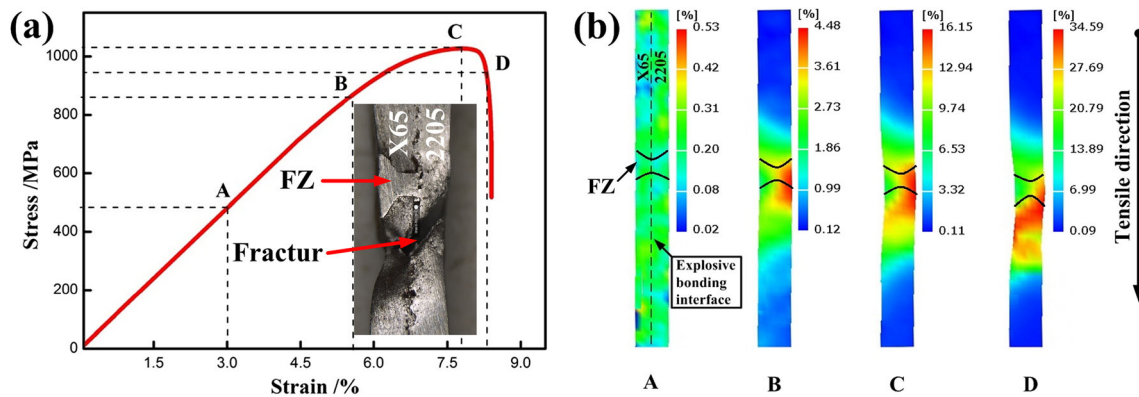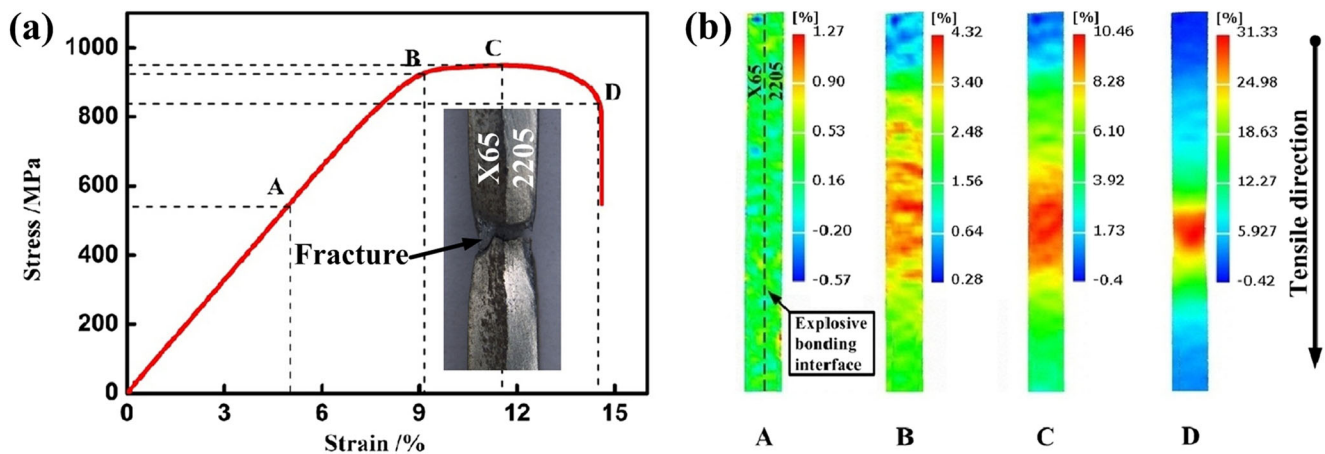

Fig. 13 a Stress-strain curves of the tensile test for the full-thickness LBW joint and the relative position of the corresponding fracture. b The corresponding localized strain distributions on the surface for the same tensile specimen at points A, B, C, and D

Fig. 14 **a** Stress-strain curves of the tensile test for the full-thickness bimetallic sheet and the relative position of the corresponding fracture. **b** The corresponding localized strain distributions on the surface for the same tensile specimen at points A, B, C, and D

specimen is shown in the inset to Fig. 14a. Figure 14b also indicates that the localized deformation is homogenous in the thickness direction, namely, in the bimetallic sheet, the parent layer X65 and the flyer layer 2205 shared the same strain distribution. This means an excellent interface bonding performance between X65 pipe steel and 2205 duplex stainless steel that was achieved through explosive welding, as also reported by Zhang et al. [24]. For the LBW joints, as demonstrated in Fig. 13b, the strain distributions reveal different characteristics. As the tensile time rises, a high strain concentration shows up in the lower FZ (i.e., 2205 side) firstly, while the upper FZ (i.e., X65 side) remains at a low local strain. The strain concentration then rises towards the parent metal near the upper FZ (i.e., X65 side), and eventually, it results in cracking and fracture. Tensile test specimen's fracture is illustrated in the inset to Fig. 13a. This result discloses that the lower FZ (i.e., 2205 side) for the LBW joints is failure's source. Besides, the fracture strain values of the lower FZ (i.e., 2205 side) are lower than that of the upper FZ (i.e., X65 side) and the bimetallic sheet. This is partly explicable by the fact that the coarse grain size in the lower FZ (i.e., 2205 side) decreases the hardness and the strength of the joint.
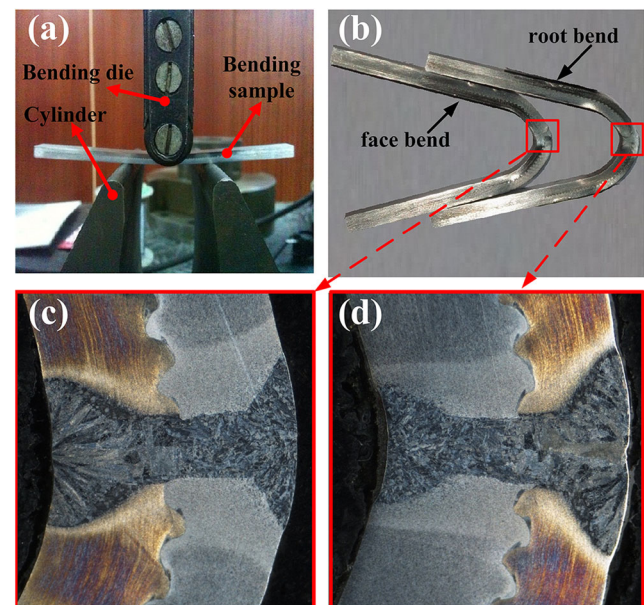
3.3.3 Bending test

A three-point bending test was applied to the LBW joint, and the bended specimens were cut from the welded plate with full thickness. In the bending tests, the diameter of the bending die was 40 mm, the diameter of the cylinder was 30 mm, and the distance between the axes of the two cylinders was 94 mm, as shown in Fig. 15a. Figure 15b shows the specimens after bending them by up to 180°. The cross section of the specimen with the maximum curvature was ground, polished, and etched before observation under an optical microscope. Figure 15c and d are the respective optical micrographs of the cross sections for the face bending and root bending

specimens of the LBW joint, which shows that separation, tearing, or fracture, did not occur around the joint after the bending test, indicating excellent bonding properties.

### 3.4 SEM analysis of the tensile shear fracture

Figure 16b shows the macroscopic fracture morphology of the full-thickness tensile test for the LBW joint. The corresponding area in the fracture surface is shown by Fig. 16a. Figure 16c–f shows a high-resolution fractography of the positions c, d, e, and f in Fig. 15b, respectively.

Figure 16c shows a dimple microscopic morphology at position c (i.e., X65), and some large dimples were distributed among numerous small dimples, which appears as a ductile

Fig. 15 Results of the three-point bending test: **a** three-point bending test, **b** the bended specimens, **c** cross-sectional view of LBW joint after face bending, **d** cross-sectional view of LBW joint after root bending
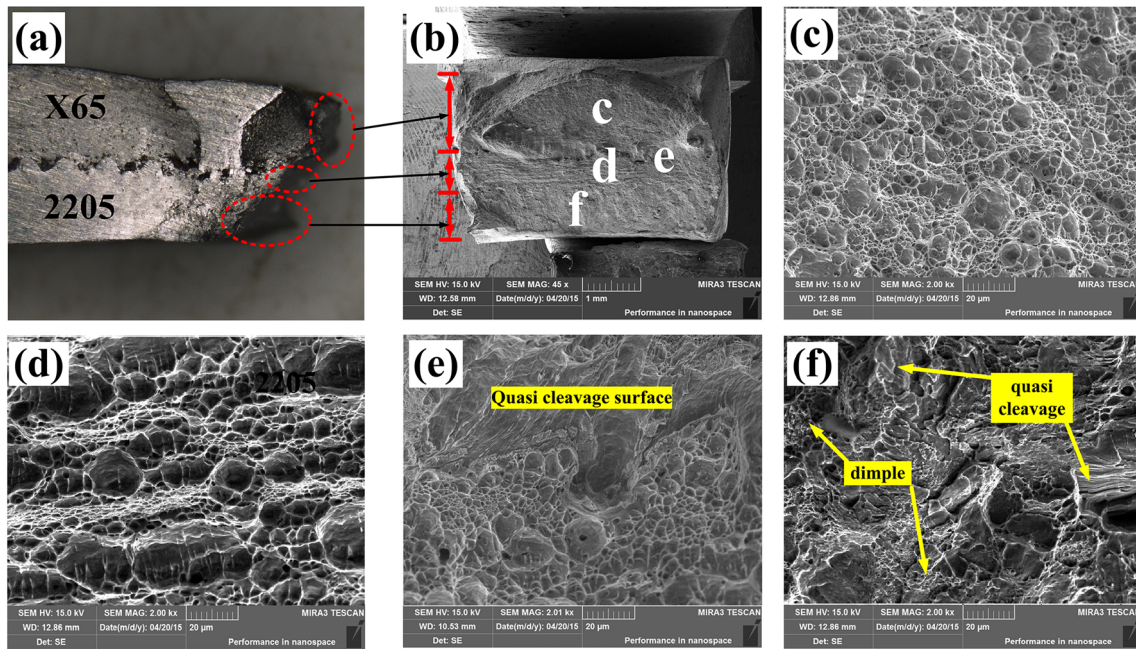
Fig. 16 Fractography of the full-thickness tensile test and of the EDS analysis of fracture: **a** relative position of the fracture, **b** macro-fractography, **c** high-resolution fractography of position c in (**b**), **d** high-resolution fractography of position d in (**b**), **e** high-resolution fractography of position e in (**b**), **f** high-resolution fractography of position f in (**b**)

fracture. Figure 16d shows the macroscopic fracture morphology of position d (i.e., 2205). The fracture surface contains ductile dimples which are formed by the microvoid coalescence mechanism and facets associated with the cleavage fracture. Position e are located on the explosive bonding interface of the two materials. From Fig. 16e, it can be seen that a quasi-cleavage fracture surface formed near the explosive bonding interface, which can be due to the columnar grain structure's fracture in the localized melted zone formed in the explosion welding process as reported by Kacar et al. [25]. Figure 16f shows that the fracture mode of the lower FZ is ductile and in quasi-cleavage mixed fracture, the dimples are believed to initiate at the second-phase particles or small inclusions within the A phase, whereas the large facets represent brittle fracture occurring along the cleavage planes of the F phase.

3.5 Corrosion properties

In the accelerated corrosion test, samples were sealed with A/B glue, leaving the lower surface of the LBW joints and BM (2205 side) as the measured surface, and the schematic diagram is shown by the inset in Fig. 17.

The polarization plots of the BM (2205 side) and LBW lower surface are shown in Fig. 17, and the corrosion current densities of BM samples and the LBW joint samples were 685.2×10^{-3} and 654.8×10^{-3} μA/cm^2, respectively. Using these corrosion current density values, the corrosion rates of the BM (2205 side) and of the LBW joint can be estimated to be 8.08×10^{-3} and 8.03×10^{-3} mm/year, respectively. The

corrosion rates of the LBW joint are slightly different from that for BM (2205 side). Such a phenomenon follows from the fact that the corrosion resistance of the LBW joint is equivalent to that of the BM (2205 side). In other words, the LBW joint lower surface can be well protected against the uniform corrosion attack through the development of a cohesive passive layer under the corrosive environment.

The polarization plot also shows that the pitting corrosion resistance of the LBW joint is worse compared to that of BM (2205 side). As can be seen from the polarization plot, the breakdown potential of the LBW joint measured from these tests is 0.26 V while the breakdown potential of the BM (2205
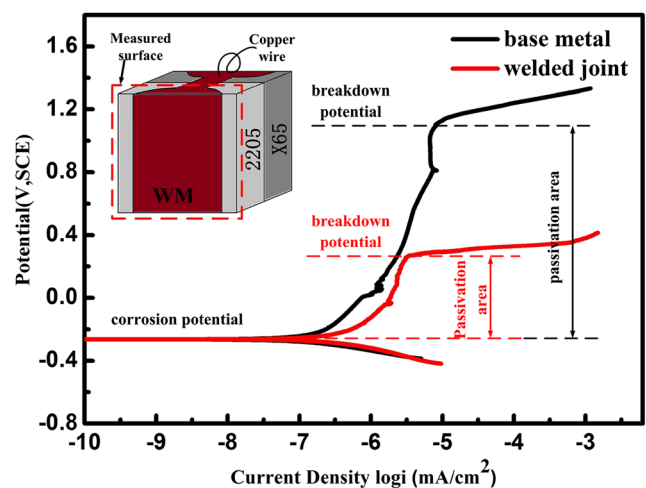
Fig. 17 Polarization curves of 2205 and LBW joint

side) is 1.1 V. Besides a small passivation area between the corrosion potential and the breakdown potential suggests poor resistance against damage nucleation in the protective layer and consequent localized corrosion attack. Such a phenomenon can be partly ascribed to the reduction of the alloying elements Cr and Ni in the LB welding process. Olsson et al. [26] reported that the alloying element Cr could improve the stability of passive films, and the Ni would decrease the overall dissolution rates of Fe and Cr. On the other hand, the heat input during welding affects a series of thermal cycles and leads to complex microstructural changes, which result in the difference of formation conditions of the metal surface passive film, such as the coarser grain and higher ferrite/ austenite rates, as described in Section 3.1.

4 Conclusions

The above-described work led us to the following conclusions:

1. Full-penetration joints without any defects were produced by the LB welding. The microstructure of the upper FZ includes martensite and bainite phases. The microstructure of the lower FZ includes networks of austenite (A) at the ferrite grain boundaries and intragranular austenite (A) precipitates, which were embedded in the continuous ferrite (F).

2. The EDS test results show that only a small amount Cr, Ni, and Mo migrated from the lower FZ to the upper FZ, whereas a small amount Fe has been moved from the upper FZ to the lower FZ.

3. The average microhardness of the upper FZ is higher than that of HAZ and BM (i.e., X65), which is attributed to the formation of martensite in the upper FZ. For the lower FZ, the average microhardness has a little lower value, as compared to the flyer plates (i.e., 2205) of the bimetallic sheets.

4. Stress-strain curves of the tensile test showed that the tensile strength is larger for the LBW joint than that for the bimetallic sheets, while the ductility was found to be smaller than that in the bimetallic sheets. The tensile test results also indicated that the fracture started at the lower FZ (i.e., 2205 side), and then it grew towards the parent metal near the upper FZ (i.e., X65 side).

5. The macroscopic fracture morphology of the lower FZ appears as a brittle fracture in stretch process. This is due to the increase in the ferrite phase and the formation of chromium-rich intermetallics or carbonitrides.

6. The lower surface of the LBW joint has higher corrosion resistance that is equivalent to that of BM (i.e., 2205); however, the pitting corrosion resistance is inferior when compared to BM (i.e., 2205). This is due to the coarser grain, the higher ferrite/austenite rates, and the reduction of the alloying elements Cr and Ni in the lower FZ.

References

1. Kaya Y, Kahraman N (2013) An investigation into the explosive welding/cladding of grade A ship steel/AISI 316L austenitic stainless steel. Mater Des 52:367–372

2. Chu Q, Zhang M, Li J, Fan Q, Xie W, Bi Z (2015) Joining of CP-Ti/ Q345 sheets by Cu-based filler metal and effect on interface. J Mater Process Technol 225:67–76

3. Imran MK, Masood SH, Brandt M (2011) Bimetallic dies with direct metal-deposited steel on Moldmax for high-pressure die casting application. Int J Adv Manuf Technol 52:855–863

4. Qwamizadeh M, Kadkhodaei M, Salimi M (2014) Asymmetrical rolling analysis of bonded two-layer sheets and evaluation of outgoing curvature. Int J Adv Manuf Technol 73:521–533

5. Kore SD, Date PP, Kulkarni SV, Kumar S, Rani D, Kulkarni MR, Desai SV, Rajawat RK, Nagesh KV, Chakravarty DP (2011) Application of electromagnetic impact technique for welding copper-to-stainless steel sheets. Int J Adv Manuf Technol 54:949–955

6. Raghukandan K (2003) Analysis of the explosive cladding of cu–low carbon steel plates. J Mater Process Technol 139:573–577

7. Gulenc B (2008) Investigation of interface properties and weldability of aluminum and copper plates by explosive welding method. Mater Des 29:275–278

8. Kahraman N, Gülenç B (2005) Microstructural and mechanical properties of Cu–Ti plates bonded through explosive welding process. J Mater Process Technol 169:67–71

9. Torbati AM, Miranda RM, Quintino L, Williams S, Yapp D (2011) Optimization procedures for GMAW of bimetal pipes. J Mater Process Technol 211:1112–1116

10. Gao XL, Zhang LJ, Liu J, Zhang JX (2013) A comparative study of pulsed Nd:YAG laser welding and TIG welding of thin Ti6Al4V titanium alloy plate. Mater Sci Eng A 559:14–21

11. Yang MX, Qi BJ, Cong BQ, Liu FJ, Yang Z (2013) Effect of pulse frequency on microstructure and properties of Ti-6Al-4V by ultrahigh-frequency pulse gas tungsten arc welding. Int J Adv Manuf Technol 68:19–31

12. Fang XY, Zhang JX (2014) Effect of underfill defects on distortion and tensile properties of Ti-2Al-1.5Mn welded joint by pulsed laser beam welding. Int J Adv Manuf Technol 74:699–705

13. Zhang LJ, Zhang JX, Gumenyuk A, Rethmeier M, Na SJ (2014) Numerical simulation of full penetration laser welding of thick steel plate with high power high brightness laser. J Mater Process Technol 214:1710–1720

14. Zhang MJ, Chen GY, Zhou Y, Li SC, Deng H (2013) Observation of spatter formation mechanisms in high-power fiber laser welding of thick plate. Appl Surf Sci 280:868–875

15. Srinivasan PB, Muthupandi V, Dietzel W, Sivan V (2006) Microstructure and corrosion behavior of shielded metal arc-welded dissimilar joints comprising duplex stainless steel and low alloy steel. J Mater Eng Perform 15:758–764

16. Young MC, Chan SLI, Tsay LW, Shin CS (2005) Hydrogen-enhanced cracking of 2205 duplex stainless steel welds. Mater Chem Phys 91:21–27

17. Yang Y, Wang Z, Tan H, Hong J, Jiang Y et al (2012) Effect of a brief post-weld heat treatment on the microstructure evolution and pitting corrosion of laser beam welded UNS S31803 duplex stainless steel. Corros Sci 65:472–480

18. Mourad AHI, Khourshid A, Sharef T (2012) Gas tungsten arc and laser beam welding processes effects on duplex stainless steel 2205 properties. Mater Sci Eng A 549:105–113

19. Sadeghian M, Shamanian M, Shafyei A (2014) Effect of heat input on microstructure and mechanical properties of dissimilar joints between super duplex stainless steel and high strength low alloy steel. Mater Des 60:678–684

20. Srinivasan PB, Muthupandi V, Dietzel W, Sivan V (2006) An assessment of impact strength and corrosion behaviour of shielded metal arc welded dissimilar weldments between UNS 31803 and IS 2062 steels. Mater Des 27:182–191

21. Liu LM, Zhuang ZL, Liu F, Zhu ML (2013) Additive manufacturing of steel–bronze bimetal by shaped metal deposition: interface characteristics and tensile properties. Int J Adv Manuf Technol 69:2131–2137

22. Bachmann M, Avilov V, Gumenyuk A, Rethmeier M (2014) Experimental and numerical investigation of an electromagnetic weld pool support system for high power laser beam welding of austenitic stainless steel. J Mater Process Technol 214:578–591

23. Findik F (2011) Recent developments in explosive welding. Mater Des 32:1081–1093

24. Zhang LJ, Pei Q, Zhang JX, Bi ZY, Li PC (2014) Study on the microstructure and mechanical properties of explosive welded 2205/X65 bimetallic sheet. Mater Des 64:462–476

25. Kacar R, Acarer M (2004) An investigation on the explosive cladding of 316L stainless steel-din-P355GH steel. J Mater Process Technol 152:91–96

26. Olsson COA, Landolt D (2003) Passive films on stainless steels-chemistry, structure and growth. Electrochim Acta 48:1093–1094